Modelling and Control of DC grids within More-Electric Aircraft

Authors: Cheng Wang, Habibu Hussaini, Fei Gao, Tao Yang

1 Introduction to More-Electric Aircraft

Increasingly moving towards More-Electric Aircraft (MEA) is one of the few existing solutions available for the development of more efficient and environmentally friendly aircraft. Driven by the development of power electronics, electric machines and advanced control technologies, many functions which were conventionally driven by hydraulic, pneumatic and mechanical power are being replaced by electrical subsystems in the MEA [1]-[4]. Such changes are shown in Figure 1(a) and Figure 1(b). Compared with conventional aircraft, the MEA offers significant cost benefits due to fewer parts, integration of key subsystems, and multi-use of components [5]. It also reduces the overall cost of operation and ownership because its more-electric architecture helps reduce fuel consumption per passenger per mile, increase overall aircraft performance and energy usage.

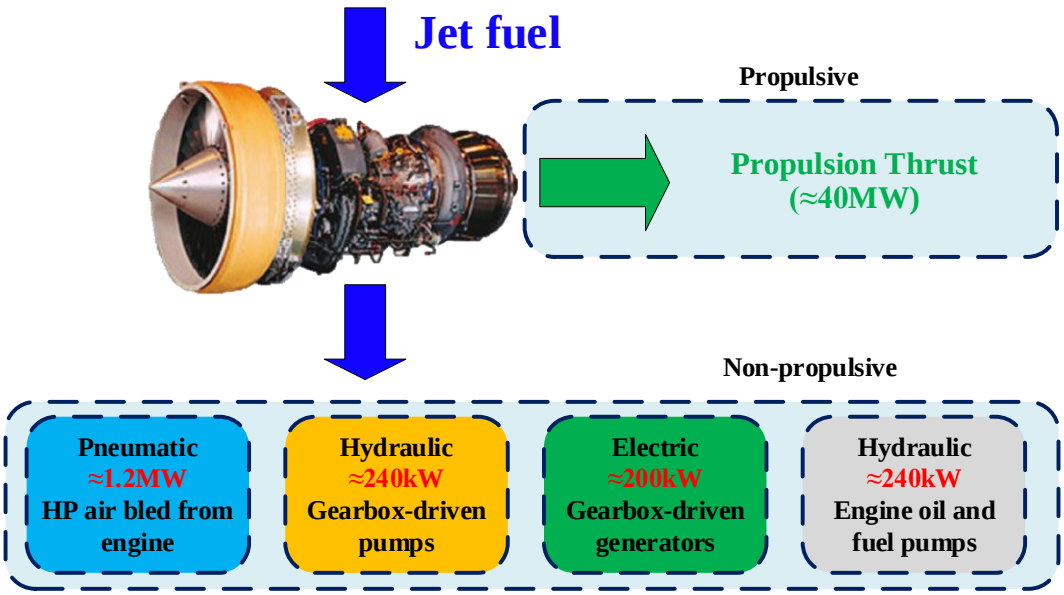

(a)

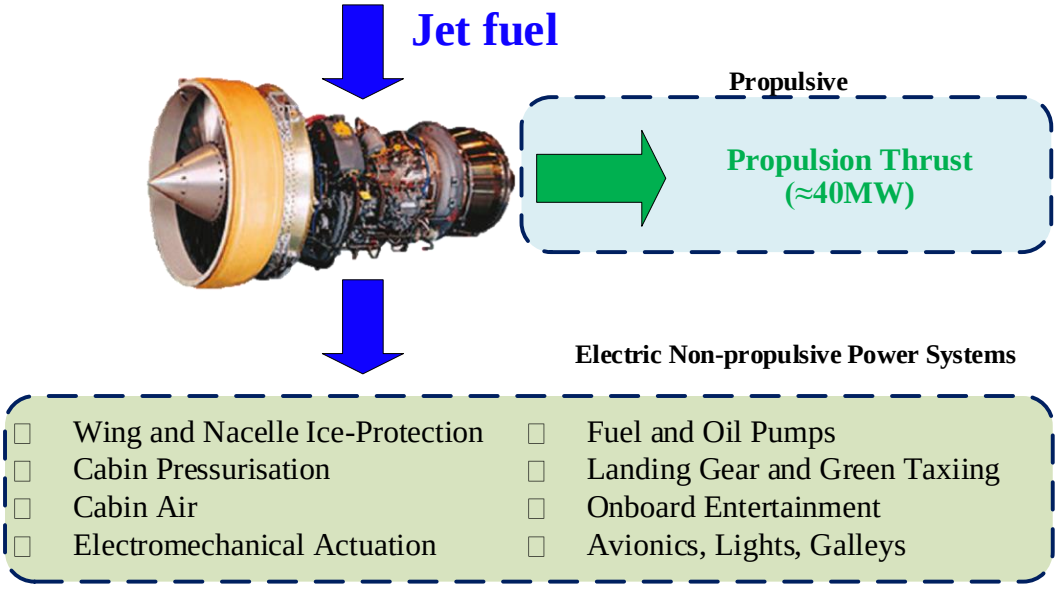

(b)

Figure 1. Change in non-propulsive power in conventional aircraft and more electric aircraft. (a) Conventional aircraft. (b) More electric aircraft.

For an increased amount of power requirement and optimal management of on-board electrical power, the concept of MEA poses increased challenges for the aircraft electrical system. Therefore, signicant attention has been focused on the electric power system (EPS) architecture design and control aspects. Many architectures have recently been proposed with performance comparison studies. A potential solution would prefer a high-voltage DC (HVDC) network architecture. The benefits of an HVDC distribution system can be summarised as follows:

- Lower losses in the power transmission cables. This is due to the fact that only two conductors (positive and negative) are required in DC distribution, whereas three conductors (three phases) are required in AC distributions [6].
- The reduction of the skin effect in DC will result in reduced power loss and dielectric losses in the power cables.
- Less corona effects with DC compared to AC conductors.
- No need for any reactive power compensation equipment. Thus the capacity of wires and devices will be increase and the cable size can be reduced because there is no need to distribute/process the reactive power [6].

- Convenience of parallelling power supplies and integrating energy storage systems (ESS).

Due to these benefits, the DC power system has attracted more attention in recent years. An example architecture of an electric grid used for the initial study is shown in Figure 2. This example EPS architecture consists of several components:

1) Generation system: The electrical power is mainly provided by two or more permanent magnet synchronous generators (PMSGs) which extract power from engine shafts. Depending on the flight scenario, the system can be operated with only one active source, or with multiple sources feeding the same DC bus.
2) Energy storage system (ESS): Energy storage system is also integrated for emergency status operation. To achieve a flexible power flow in the system, a bi-directional DC-DC converter is implemented. Therefore, the discharge and charge mode of the battery can be controlled.
3) Load: The onboard loads are represented by a combination of conventional resistive loads and by constant power load (CPL) typically driven by tightly controlled power electronic devices. Here, a permanent magnet synchronous machine (PMSM) drive is used to represent electromechnical actuation system, which is essentially one type of CPLs.

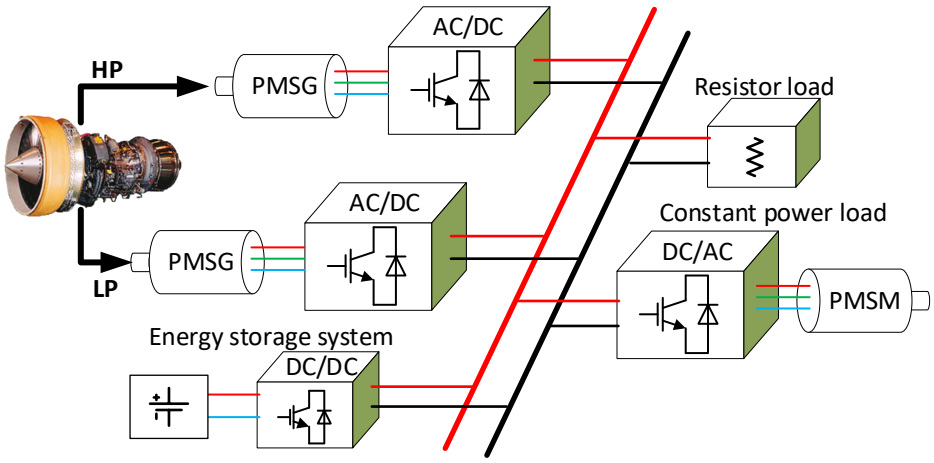

Figure 2. Typical DC-grid in Electric Aircraft

2 Modelling of Aircraft EPS

Application of the MEA concept will see significant penetration of Power Electronic

Converters (PEC) into aircraft EPS. These PECs and their control systems will lead to significant challenges for EPSs designers. To ensure system stability, availability and power quality issues, the modelling and simulation of the EPS are required.

2.1.1 Multi-level Modelling Paradigm

Modelling of the electrical power system element has been studied for decades. The model required for EPS studies is always dependent on its application. Figure 3 categorises the EPS model into four levels: architecture level, functional level, behavioural level and component level [7]. The complexity of the model increases from the top architecture-level models to the bottom component-level models.

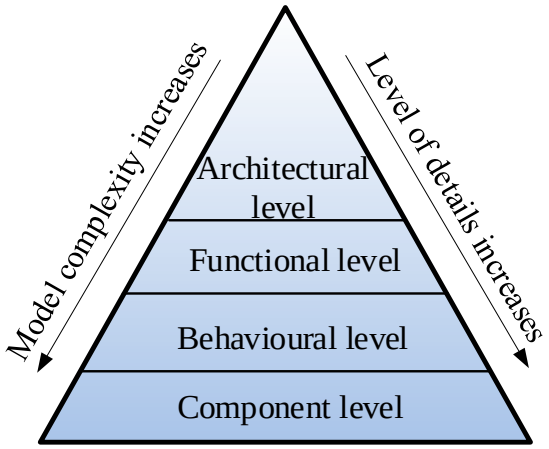

Figure 3. The multi-level modelling paradigm [8]

(a) Component level

The bottom component layer aims to model the behaviour of components within a subsystem, especially critical components. Component models cover high frequencies, electromagnetic field and electromagnetic compatibility (EMC) behaviour, and perhaps thermal and mechanical stressing. The modelling bandwidth of component models can be up to MHz if required.

(b) Behavioural level

The behavioural layer model uses lumped-parameter subsystem models, and the modelling frequencies can be up to hundreds of kHz. Models in this level cover the converter switching behaviour and the impact of harmonics. The nonlinearities and the dynamics of the subsystem up to the switching frequency are preserved in the

behavioural model.

(c) Functional level

The next level is generally known as the functional level where system components are modelled to handle the main system dynamics up to 150Hz, and the error should be less than 5% in respect of the behaviour model accuracy [8]. The functional-level model is targeted at the study of overall power system performance, stability, transient response to loading and start-up, and aims to model the power system either in its entirety or in sections sufficiently large to obtain a holistic generator-to-load dynamic overview. Since the model complexity of the functional model is reduced, the computation time of the functional model is aimed at that approaching the real simulated time. The model developed in this chapter will be targeted at this level, and a model library suitable for the simulation study of the future MEA power system will be established.

(d) Architecture level

The top architectural layer computes steady-state power flow and is used for weight, cost and cabling studies [9]. The model in this level also allows event modelling such as bus configuration and step of loading, and reliability, stability and availability studies. The architectural models are the simpler ones and are representative only of steady-state power consumptions.

2.1.2 Studies of Functional Models

Modelling and simulation of EPS are essential steps that enable the design and verification of numerous electrical energy systems including the modern electric grid and its components, distributed energy resources, as well as electrical systems of ships, aircraft, vehicles and industrial automation. With the increasing use of power electronic devices, it is impractical to simulate and study such a complex system with detailed component-level device models or behavioural device models. As these models include high bandwidth components, from kHz to MHz, very small simulation steps and a huge amount of computer memory are required. This leads to significant simulation time and makes the large-scale EPS simulation at these two lower levels impractical. In addition, these two lower-level models are discontinuous and therefore are difficult to use for extracting the small-signal characteristics of various modules for system-level analysis

[10]. The above challenges have led to the development of average modelling techniques; these can be categorised at the functional level.

The Average-Value Modelling (AVM) method removes the effect of the switching behaviour of the power electronic device using the dynamic average values of the variables. Due to fact that the switching frequency of the electronic power converters is much higher than the system dynamics, the system-level study can be conducted with the dynamic average value defined over the length of a switching interval, instead of looking at the instantaneous values of currents and voltages that contain ripples due to switching behaviour of PECs. The dynamic average value of a time-domain variable $x(t)$ is defined as

$$\overline{x} = \frac{1}{T_s} \int_{t-T_s}^{t} x(t)dt \tag{1}$$

where T_s is the switching period. For the DC/DC converters, $x(t)$ may represent the input or output voltage $v(t)$ and current $i(t)$. The AVM of PWM DC/DC converters can be given in either an analytical or equivalent circuit form using the definition (1). Theoretically, these two forms of models are equivalent for any given converter topology. As shown in Figure 4, the left side shows a switched cell commonly used in a DC/DC converter; the right side shows its equivalent circuit. In the average model, the switch pair, an IGBT and a diode are replaced with dependent sources which are functions of the duty cycle and the averaged values of the cell's terminal variables [11][12].

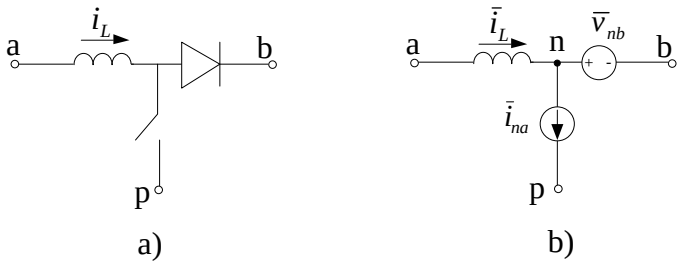

Figure 4. Switched-inductor cell and its averaged circuit model

In the analytical AVM for the PWM DC/DC converter, the state equations for each topology within a switching interval T_s are firstly obtained. Using (1), the final average

model is then derived from the weighted sum of the state-space equations for different subintervals.

This concept of averaging has also been extended to modelling AC/DC and DC/AC converters. However, instead of directly averaging the AC variables using (1), the AC side variables are transformed into a synchronous rotating reference frame, referred to as the *dq* frame [13]. In the *dq* frame, the three-phase AC variables are transformed to be composed of a DC (constant) term and high-frequency ripples with the same switching interval. Because the variables have the DC component that is constant in the steady-state, these variables can be used for averaging using (1). Compared with original signals, the DC-like averaged signals allow the variable-step solver to choose bigger simulation steps under the same tolerance condition.

Instead of deriving the AVM model by averaging variables after the *dq* transformation, the calculation of AVM models of AC/DC or DC/AC converters can use the converse process, i.e. pre-processing the AC variables and then using the *dq* transformation. This method neglects all the switching higher harmonics and only considers the fundamental component of the AC variables and the switching functions. The variables on the AC and DC sides are related through the fundamental components of the switching functions. The application of the *dq* transformation on these fundamental components gives the AVM model of the AC/DC or DC/AC converters. This method will give the same result as that obtained from the first one and is more applicable in the modelling of an EPS. In this chapter, it will be referred to as the DQ0 modelling technique. The DQ0 modelling technique is based on the fact that the DC component in the *d* and *q* axis is only derived from the fundamental components of the AC variables. The DC component of the DC-side variables is also only dependent on the fundamental components of the AC-side variables and the switching functions. The DQ0 model has been successfully used in the modelling of the More Open Electrical Technologies (MOET) aircraft EPS [14]-[16]. There the DQ0 model has been proved to be an effective way to study a large-scale EPS with high accuracy and computation efficiency, especially under balanced conditions where the DQ0 model simulates more than 1000 times faster than the corresponding behavioural model. It is, so far, one of the most efficient models in EPS studies. In this chapter, the DQ0 model is used for comparison

studies. The efficiency of the DQ0 model, however, decreases dramatically when the system is under unbalanced conditions. This is due to the negative sequence present in the system. In the DQ0 model this negative sequence will become the second harmonic in the *d*- and *q*-axis variables. Since the *dq* variables are no longer constant in the steady-state, the simulation speed becomes much slower and is comparable to simulating with non-transformed AC variables.

2.2 Modelling of Power Generation System

This section focuses on the modelling of components in the MEA EPS. As illustrated in the previous section, functional models are used because of their effectiveness.

2.2.1 Permanent Magnet Synchronous Generators

The 3-phase permanent magnet synchronous generator (PMSG) is one of the most widely used generators in DC grids in recent decades. Figure 5 shows a PMSG developed by the University of Nottingham within the CleanSky AEGART project [17]. This project aimed to develop an electrical starter/generator system for next-generation business jet applications.

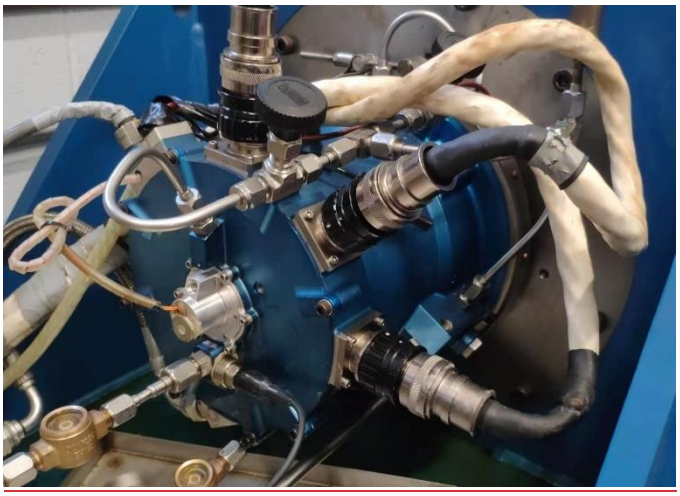

Figure 5. PMSG developed within AEGART project.

To avoid the complexity associated with the calculation of 3-phases, it is widely adopted that PMSG can be modelled with a synchronously rotating reference frame (*dq* frame). The dynamic equations for PMSG in the *dq* frame are as expressed in (2).

$$\begin{cases} v_d = Ri_d + L_d \dfrac{di_d}{dt} - \omega_e L_q i_q \\ v_q = Ri_q + L_q \dfrac{di_q}{dt} + \omega_e L_q i_q + \omega_e \varphi_m \end{cases} \quad (2)$$

where v_d, v_q, i_d, i_q, L_d, L_q, R, φ_m, ω_e represent d-axis stator voltage, q-axis stator voltage, d-axis current, q-axis current, d-axis inductance, q-axis inductance, stator resistance, flux linkage of the permanent magnet, and electrical rotor angular velocity respectively. Model diagram based on (2) is shown in Figure 6.

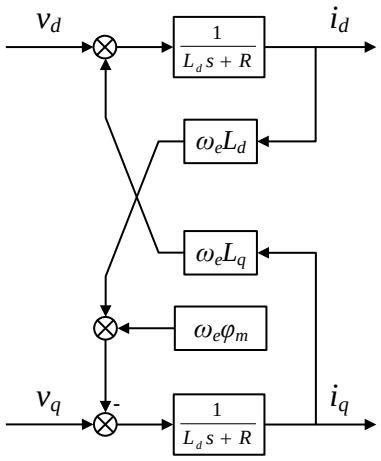

Figure 6. Model of PMSG

In MEA EPS, surface mounted PMSG is always used because of its mechanical benefit for high-speed operation. Then, the *d*- and *q*-axis inductances are considered to be identical (L_d=L_q=L_s) in the case of the surface-mounted PMSG [17]. Therefore, the equation (2) can be re-written as the expression in (3).

$$\begin{cases} v_d = Ri_d + L_s \dfrac{di_d}{dt} - \omega_e L_s i_q \\ v_q = Ri_q + L_s \dfrac{di_q}{dt} + \omega_e L_s i_q + \omega_e \varphi_m \end{cases} \quad (3)$$

Maximum allowable phase currents are determined by designed rated parameters of the converter and machine. Maximum voltage is dependent on the available DC-link voltage and modulation method. The voltage and current limitations can be written as in (4) by neglecting stator resistance and the transient terms.

$$\begin{cases} \omega_e \sqrt{\left(L_s i_q\right)^2 + \left(L_s i_d + \varphi_m\right)^2} \le v_c^{max} \\ \sqrt{i_d^2 + i_q^2} \le i_c^{max} \end{cases} \tag{4}$$

where v_c^{max} and i_c^{max} are the maximal phase voltage amplitude at the fundamental frequency and maximal phase current, respectively.

2.2.2 AC/DC Power Converters

Due to increased onboard electrical power, high power quality is one of the requirements for the AC-DC power conversion in MEA. As a potential substitute for traditional transformer rectifiers, the active-front-end converters (AFE) can get better electrical behaviour and keep the same performances in robustness and safety requirements. For aircraft applications, the topology of the AFE converter can potentially be two-level and three-level converters (especially the neutral point clamped topology) as shown in Figure 7. A two-level converter was considered for its known simplicity and intrinsic reliability due to the minimal number of devices. A three-level converter was also considered because it brings advantages of lower electromagnetic interference emissions, better power quality and the ability to handle higher fundamentals compared with two-level converters [20]. These are useful features when considering the high-speed application (for example aircraft electric starter/generator which is driven by an aircraft engine shaft). In addition, the voltage across the switches is only half the dc bus voltage. This feature effectively doubles the power rating of the converter for a given power semiconductor device.

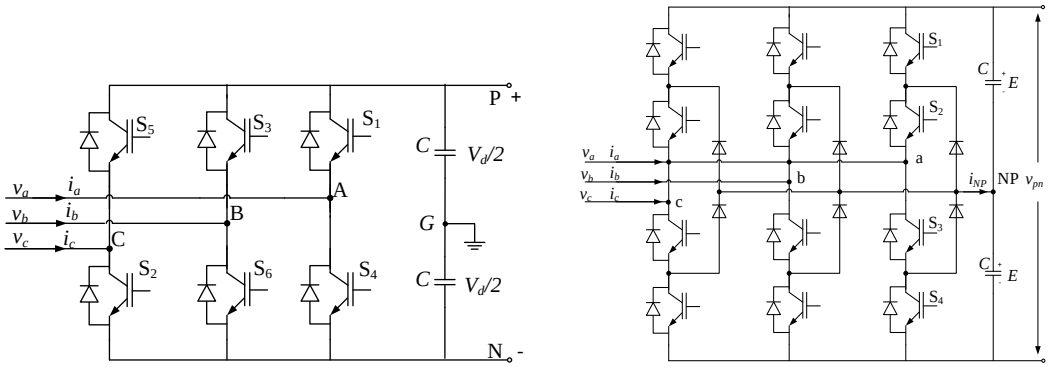

Figure 7. Active front-end rectifier (AFE). a) Two-level three phase AFE. b) Three-level three phase AFE.

Figure 8 shows an active front-end based on a three-level neutral point clamped (NPC) converter developed by the University of Nottingham within the CleanSky AEGART project [17].

Figure 8. A three-level converter developed in the University of Nottingham within Clean Sky AEGART project

Such AC/DC converters are also essential elements for electric actuation devices, namely electro-mechanical actuators (EMAs), which will potentially replace the conventional hydraulic powered actuators to meet the target of removing hydraulic systems.

The control scheme utilised in this chapter will be field-oriented control (FOC) in which the stator currents of a three-phase AC electric motor are identified as two orthogonal components that can be visualized with a vector. The rotating reference, (or *dq*) frame, which is part of FOC will be detailed. Figure 9 shows the phasor diagram of the three-phase stationary and two-phase rotating *dq* frames. $v_{a,b,c}$ represent the three-phase frames of phase voltages, $v_{d,q}$ represent the *dq* frames, and θ is the angle between both frames.

The frame transformation from three-phase to *dq* can be interpreted into a set of mathematical equations. If the *d*-axis is aligned with phase *a* ($v_d = v_a$) as a reference point for both frames (θ=0), then:

$$\begin{bmatrix} v_d \\ v_q \end{bmatrix} = k_{dq} \begin{bmatrix} v_a \\ v_b \\ v_c \end{bmatrix} \tag{5}$$

$$k_{dq} = \frac{2}{3}\begin{bmatrix} \cos(\theta) & \cos\left(\theta - \frac{2\pi}{3}\right) & \cos\left(\theta + \frac{2\pi}{3}\right) \\ -\sin(\theta) & -\sin\left(\theta - \frac{2\pi}{3}\right) & -\sin\left(\theta + \frac{2\pi}{3}\right) \end{bmatrix} \tag{6}$$

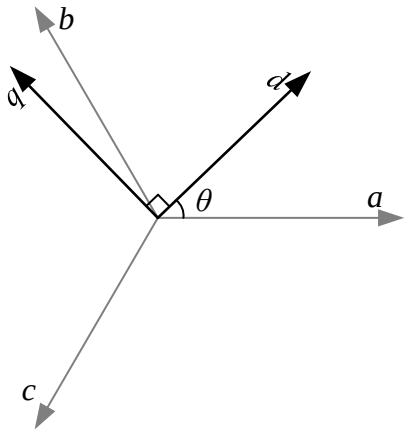

Figure 9. Three phase and *dq* phasor diagram.

Now, the converter is also modelled in *dq* frame. The converter's AC voltage v_c can be expressed as

$$v_c = \sqrt{v_d^2 + v_q^2} \tag{7}$$

As shown in Figure 10, the d-axis and q-axis components of the AC-side terminal voltage can be written as in (8) and (9).

$$v_d = \frac{1}{2} m_d v_{dci} \tag{8}$$

$$v_q = \frac{1}{2} m_q v_{dci} \tag{9}$$

where m_d, m_q are the modulation indices in corresponding directions.

The AC-side terminal real power of the two-level AFE can be formulated as in (10).

$$P = \frac{3}{2}\left(v_d i_d + v_q i_q\right) \tag{10}$$

If neglecting the power losses of the converter, as shown in Figure 10, the power

balance between the DC and AC side yields the expression in (11).

$$V_{dc} i_{dc} = \frac{3}{2}\left(v_d i_d + v_q i_q\right) \tag{11}$$

where i_{dc} is the output DC current flowing after the capacitor.

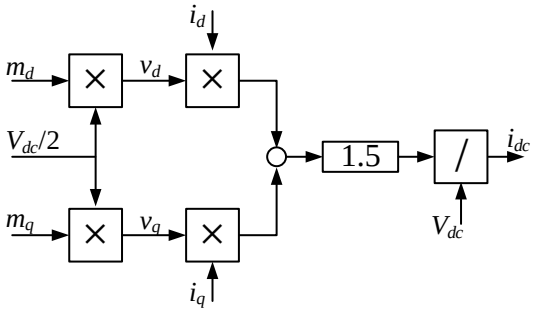

Figure 10. Model of AC-DC converter

2.3 Energy storage system

The energy storage system (ESS) provides power for starting PMSG and it also absorbs the excess power generated by the PMSG. During an emergency (loss of normal electrical power supply from the PMSG(s)), the ESS can provide power to the loads for a limited time through a bidirectional DC-DC converter. Furthermore, the ESS can help meet the increasing onboard power demand without installing additional generators. This will be of great advantage in terms of the aircraft fuel economy [18]. Several technologies are currently used for energy storage. These include mechanical, hydraulic, electro-chemical and pneumatic technologies [19][20]. The ultracapacitors, lead-acid batteries, flow batteries and lithium-ion batteries are the common energy storage system solutions among the electro-chemical technologies [19][20]. Batteries have the advantage of higher charge efficiency, ease of installation, cost-effective, and responsiveness when compared with other storage systems. Specifically, the lithium-ion batteries show about 99% charge efficiency, and 86-99% energy efficiency, depending on the charge and discharge C-rate (a measure of the rate at which the battery is discharged in relation to its maximum charge) [21]. On the other hand, other energy storage systems, for example, fuel cells, have only about 66% efficiency [22]. Also, batteries can deliver power immediately, unlike fuel cells that need a few minutes before generating power. Batteries find application in the establishment of standalone

renewable power systems which are utilized for remote energy generation. The energy storage device (ESD) or system (ESS) helps to store and give out energy based on the generator and load profiles [23][24].

Figure 11 shows a typical ESS. A bi-directional DC-DC converter (buck-boost type) is chosen here due to its simple structure with higher reliability compared to other converters.

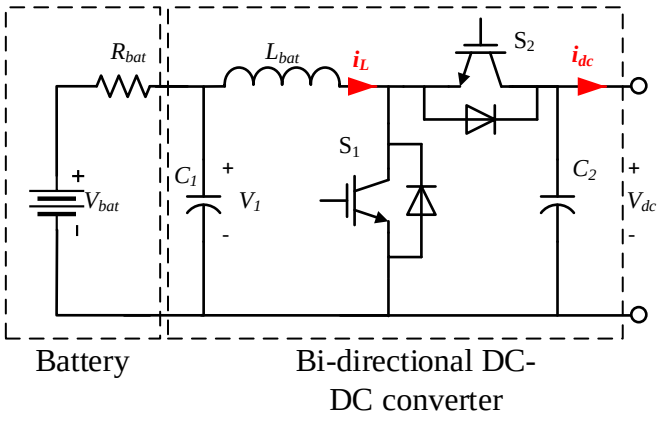

Figure 11. Energy storage system

2.3.1 Battery

In general, the battery bank module comprises of battery cells connected in series and parallel to achieve the desired voltage and power level. As shown in Figure 11, a simple model of a constant voltage source V_{bat} in series with a resistor R_{bat} is used to represent the battery.

The battery voltage is always determined by the state of charge (SOC) shown in Figure 12. There have been several computation methods for both SOC and battery voltage. The methods used vary and are dependent on the category of the battery. Hence, it will not be discussed in detail here.

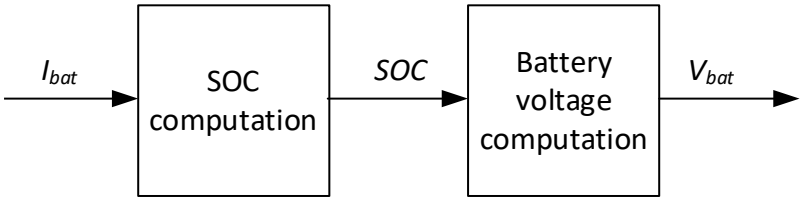

Figure 12. Battery model overview

2.3.2 Bidirectional DC-DC converter

A Bidirectional DC-DC converter allows both charge and discharge modes of the battery bank by modifying the switching duty cycle of power electronics devices. An average model per switching period is considered here.

The topology of the bidirectional buck-boost converter has been shown in Figure 11. When the converter operates in boost mode (discharging mode), the magnitude of the converter's output current at the DC link i_{dc} is positive. In contrast, it is negative when it operates in buck mode (charging). It is assumed that the converter's inductor always operates in continuous conduction mode. Then, the model can be depicted as expressed in (12), (13) and (14).

$$\frac{dV_1}{dt} = \frac{-V_1 + V_{bat}}{C_1 R_{bat}} - \frac{i_L R_{bat}}{C_1} \tag{12}$$

$$\frac{dV_{dc}}{dt} = \frac{(1-d)i_L - i_{dc}}{C_2} \tag{13}$$

$$\frac{di_L}{dt} = \frac{-V_1 + (1-d)V_{dc}}{L_{bat}} \tag{14}$$

where V_{bat} and R_{bat} are the internal voltage and resistance of the battery bank, C_1 and C_2 are the capacitance at the battery bank side and DC link side, V_1 is the voltage on capacitor C_1, L_{bat} is the bi-directional buck-boost inductor and the current through it is i_L.

2.4 DC link modelling

The dynamics on the DC-link can be expressed as in (15)

$$\frac{dV_{dc}}{dt} = \frac{i_{dc} - i_o}{C_b} \tag{15}$$

Here, i_{dc} is the current generated from sources, i_o is output current for loads, C_b is the capacitance of DC-link. If the impedance of the DC cable between the converter and the main DC bus is ignored, V_{dc} is equal to the main bus voltage (V_b). The nominal voltage of the main bus is always defined based on a certain standard. For instance,

270V is the nominal voltage and a range between 250V and 280V is acceptable for the more electric aircraft (MEA) as defined in MIL-STD-704F.

2.5 Load modelling

Onboard conventional aircraft, electric power mainly supplies energy for avionics, lights, entertainment, and galleys. With the development of power electronics, MEAs introduce new kinds of electric load, such as air conditioning and pressurisation, flight controls, fuel pumps and wing ice protection.

2.5.1 Environmental control system

Environmental control system (ECS) is one of the largest power consumption and non-propulsive systems for civil aircraft. It provides air supply, thermal control and cabin pressurization for the crew and passengers.

As shown in Figure 13(a), ECS in conventional aircraft is designed to rely on the air bled from the engine, to achieve the required temperature and pressure of the cabin air. However, the air bled from the engine will reduce the operating efficiency of the engine. For that matter, large amounts of energy will be wasted after the power optimization process of ECS.

ECS under the MEA environment is shown in Figure 13(b). Compared with Figure 13(a), the ECS converts the power extraction source from the bleed air to the electric power. Such electric power is generated by electrical motors (mostly PMSMs) with adjustable speeds. Therefore, it can realize a variable temperature and pressure control of the cabin air [25][26].

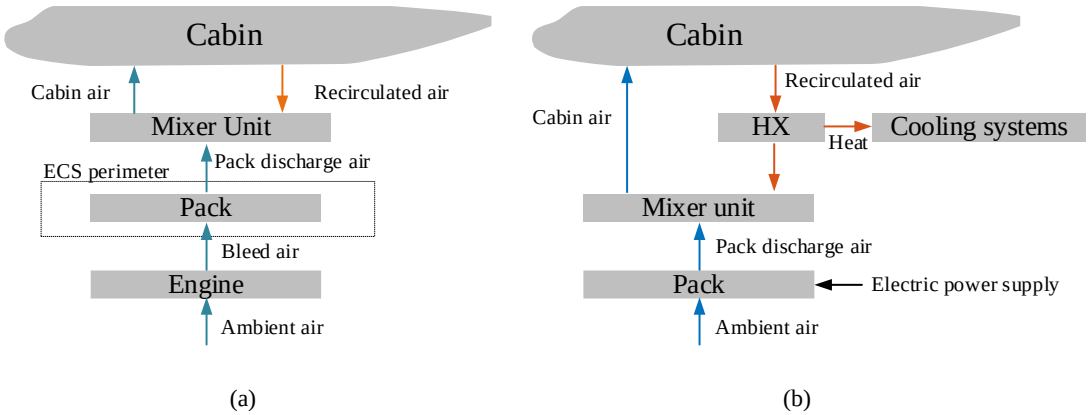

Figure 13. ECS in conventional aircraft and MEA. a) Conventional aircraft. b) MEA.

2.5.2 Flight controls

Flight controls of aircraft are performed with a variety of control surfaces or mechanisms. Generally, modern aircraft actuation systems including primary control surfaces, secondary control surfaces, landing gear system are powered by a combination of a hydraulic, pneumatic, and mechanical system. With the development of power electronics, electro-mechanical actuator (EMA) has the potential to replace the hydraulic actuators, which brings the benefits of weight reduction, improved maintainability, and the potential advantage of more flexible flight control by introducing distributed actuation system architecture [27].

Figure 14 shows a conceptual diagram of EMA. In such a system, each turn of the motor moves the actuator a fixed amount. A direct connection between the motor and actuator arm is achieved. Potentially, the EMA will be the most compact solution for flight controls.

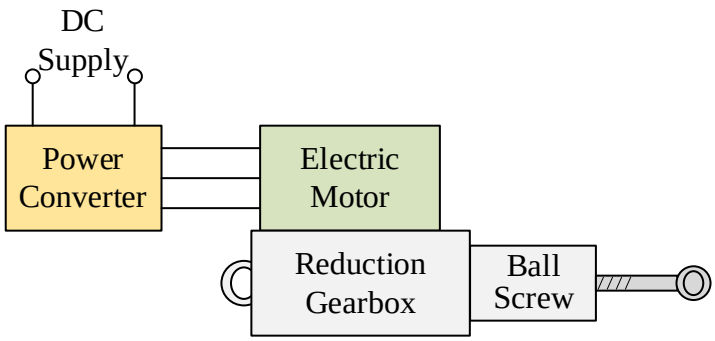

Figure 14. Electro-mechanical actuator.

2.5.3 Fuel pumps

In the MEA, fuel pumps are driven by electric motors, instead of the accessory gearbox as in current aircraft. As electrical loads, fuel pumps pressurise and feed the fuel to the engine. Meanwhile, some fuel pumps also transfer fuel between the tanks and the collector tanks to modify the aircraft centre of gravity position and reduce wing bending and structural fatigue within the wing.

In B787, the engine-driven pumps (EDP) are replaced by electrical pumps giving a total load of 400kVA.

2.5.4 Wing ice protection

One of the new electric loads onboard MEA is the wing ice protection system (WIPS), which employs electrically produced heating using resistive thermal mats. In larger aircraft, the WIPS can typically demand about 125 kW per wing [28][29].

2.5.5 General load model

As illustrated in previous sections, many kinds of loads are controlled by power electronics, such loads include ECSs and EMAs. Using EMA as an example, the output power of one EMA can be expressed as

$$P_{EMA} = T_{EMA}\omega_{EMA} = \text{const} \tag{16}$$

where P_{EMA}, T_{EMA} and ω_{EMA} represent the output power, output torque and rotor speed of EMA. In the EMA control system, T_{EMA}, ω_{EMA} are always constant, thus EMA gives a CPL performance in the EPS.

Therefore, the load power in the electric aircraft DC grid is made up of a combination of constant impedance load (wing ice protection load) and constant power load (CPL) in general. The combination can be expressed as in (17).

$$P_L = P_{res} + P_{cpl} = \frac{v_b^2}{R_{res}} + P_{cpl} \tag{17}$$

where P_{cpl} and P_{res} are the total power of the CPL and resistive load, R_{res} is the resistance of the resistive load. Then, the voltage-current relationship can be written as in (18).

$$i_o = \frac{v_b}{R_{\text{res}}} + \frac{P_{\text{cpl}}}{v_b} \tag{18}$$

In simulation studies, CPL can be simply represented as a controllable current source. The model diagram of the load combination is shown in Figure 15.

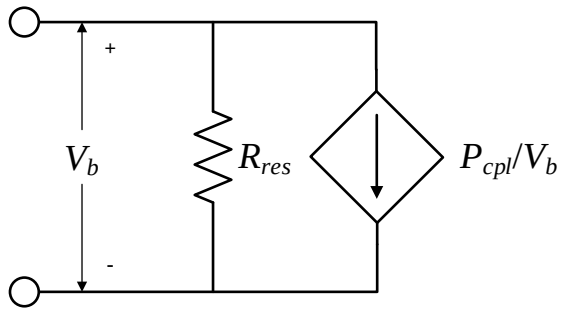

Figure 15. Load model (constant impedance load + constant power load)

3 Control development

Effective control strategies should be developed to achieve stable and efficient operation of the dc grid in MEA. As shown in Figure 2, the DC grid in MEA consists of a number of parallel converters that work together. A local controller (LC) is needed for each converter to generate the required voltage or current for the system stably. Meanwhile, a high-level control method is required to coordinate the controller among sources

3.1 Single PMSG control

This section will detail the control design for a single generation system based on models illustrated in section 2.1. Based on the aforementioned, the detailed control scheme for generator mode is as shown in Figure 16. The flux-weakening (FW) controller and DC controller generate the *dq*-current references which are fed to the current controller as shown in Figure 16.

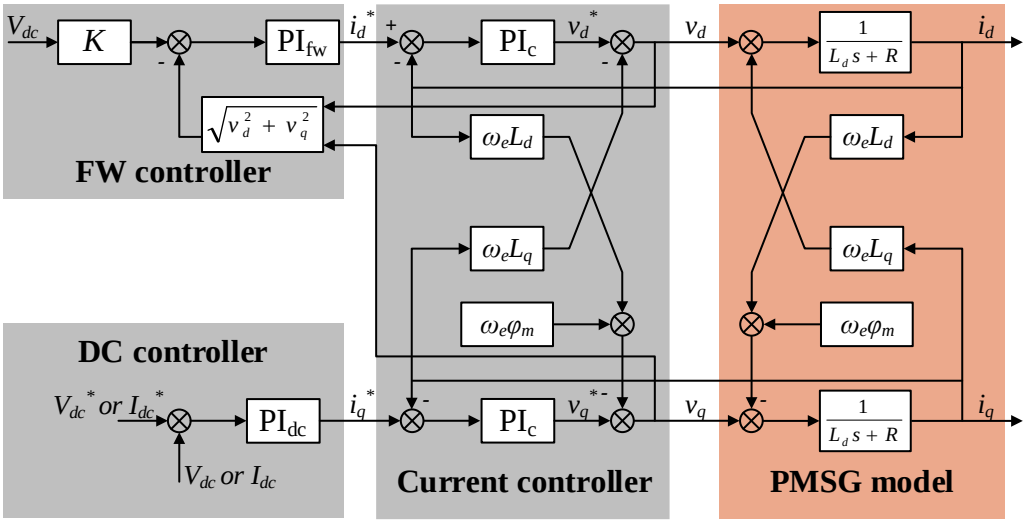

Figure 16. Control block diagram of PMSM

3.1.1 Current control Loop

The first stage is to design the current controllers of the starter generator (S/G) power system. It controls *dq*-current (i_d and i_q) following their reference (i_d^* and i_q^*). Figure 16 shows the *dq* current loops and their respective control plant. The feedforward terms within the current control plant are used for the compensation of the coupling effect in the dq frame. Then it can be reduced to a first-order transfer function as expressed in (19) and (20) for the d-axis and q-axis current respectively.

$$\frac{i_d}{v_d^*} = \frac{1}{L_s s + R} \tag{19}$$

$$\frac{i_q}{v_q^*} = \frac{1}{L_s s + R} \tag{20}$$

Applying a PI controller with feedforward elements, a closed-loop transfer function can be derived as

$$\frac{i_d}{i_d^*} = \frac{k_{pc} s + k_{ic}}{L_s s^2 + \left(R + k_{pc}\right) s + k_{ic}} \tag{21}$$

$$\frac{i_q}{i_q^*} = \frac{k_{pc} s + k_{ic}}{L_s s^2 + \left(R + k_{pc}\right) s + k_{ic}} \tag{22}$$

where k_{pc} and k_{ic} are the proportional and integral gains of the current regulator. The transfer function is similar to an ideal second-order response, which can be written as

$$\frac{\omega_n^2}{s^2 + 2\xi\omega_n s + \omega_n^2} \tag{23}$$

where ζ is the damping ratio, and ω_n is the natural bandwidth. For the current regulator, ζ and ω_n can be expressed as in (24) and (25), respectively.

$$\omega_n = \sqrt{\frac{k_{ic}}{k_{pc}}} \tag{24}$$

$$\xi = \frac{R + k_{pc}}{2L_s\omega_n} \tag{25}$$

To achieve the desired dynamic and statistic response, the values of ζ and ω_n are always set according to fundamental frequency and switching frequency. Then proportional and integral gain of the current regulator can be calculated.

3.1.2 DC link control and flux weakening control

After designing the current controller, the *dq*-current references are discussed here which are generated from flux weakening controller and DC-link controller as mentioned earlier.

The flux-weakening controller remains active during generator mode in order to maintain the stator voltage (|V|) at the required level and avoid overmodulation of the converter. When the machine rotates beyond the base speed, the flux-weakening operation is activated, and a negative d-axis current (i_d^*) is injected based on the error between the reference voltage and the voltage limit set by the converter.

The q-axis current reference is set by the outer DC power loop when the system operates in the generation mode. During the flight, the system operates in the generation mode and the q-axis current reference (i_q^*) is set by the dc-link current or voltage demands dictated by the specific power sharing method. For instance, the current reference should be implemented when the power sharing method is voltage feedback-based droop control (current-mode droop control method). In contrast, voltage reference

should be implemented when the power sharing method is current feedback-based droop control (voltage-mode droop control method).

In Figure 16, the control value of i_q^* is determined by the flux-weakening controller due to the function of the dynamic limiter prioritising FW control signals.

3.2 ESS control

The controller for the bi-directional DC-DC converter is as shown in Figure 17. Two PI controllers are connected in cascaded form and used to obtain the duty cycle (d) for switches.

In practice, the DC-link voltage controller can be eliminated when the voltage regulation is carried out by other sources.

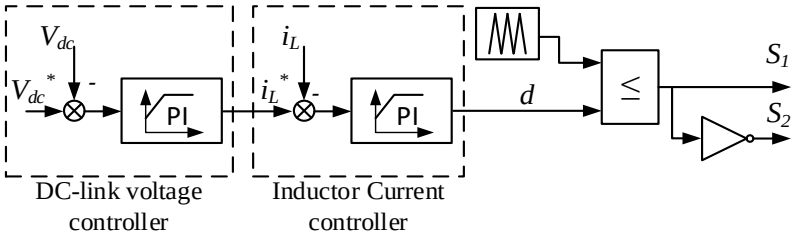

Figure 17. ESS controller

3.3 Power sharing control

After discussing each local controller (LC) in the electric aircraft's DC grid, it is essential to manage the power sharing among multiple generators. When a proper power sharing control method is implemented, system-level optimization such as efficiency improvement, power management can be achieved/realized.

Based on communication usage, multi-source control can be divided into 3 categories: centralized control, distributed control, and decentralized control. These methods are briefly discussed as follows.

3.3.1 Centralized control

As shown in Figure 18, centralized control can be implemented in a distributed generation (DG) based DC grid by employing a centralized controller. Data from DG are collected in a centralized aggregator, then processed and feedback commands are sent back to them via a digital communication network which is shown as dash lines in

Figure 18.

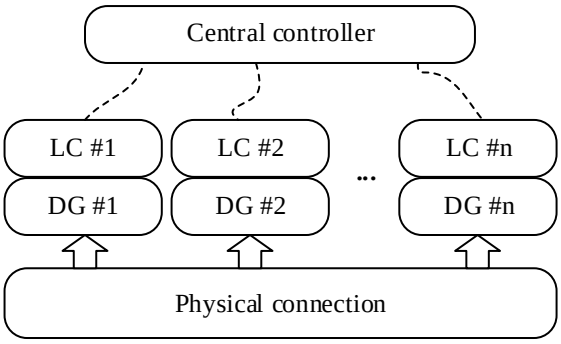

Figure 18. Operation principle of centralized control

It is easy to apply a centralized controller in a small scale grid system. Figure 19 shows a typical scheme of it. The centralized controller regulates the DC bus, thereafter current references for each power module are generated by splitting the total current reference according to the rated power ratio of sources.

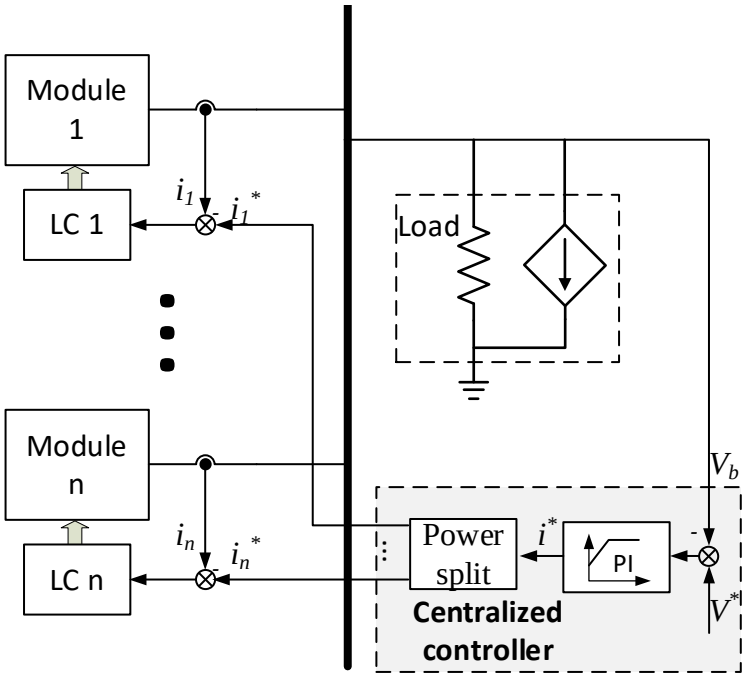

Figure 19. Control scheme of centralized control.

In some cases, master-slave control can be implemented as an alternative to centralized control. It is realised by a module chosen as a “master” and remaining modules as “slaves”. Normally the module which has the largest capacity or is the most reliable can be chosen as a “master”. The master module regulates the DC-link voltage and

generates the current references for the remaining “slave” modules. The typical block diagram of master-slave control is illustrated in Figure 20.

Compared to the centralized controller, master-slave control is more difficult to apply. However, it minimizes the use of an extra centralized controller, which helps reduce the system cost.

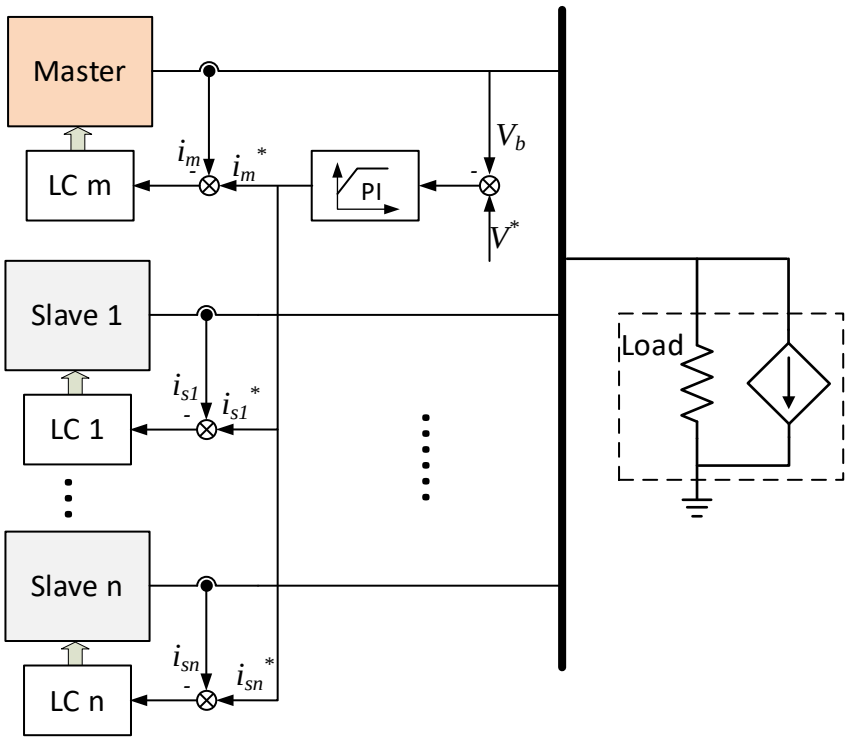

Figure 20. Control scheme of master-slave control.

Although centralized control has much better voltage regulation and current sharing performance, the requirement of communication restricts its application area such that it cannot be used in large-scale systems.

3.3.2 Distributed control

As shown in Figure 21, there is no central control unit in a distributed control system. Communication lines only exist between the neighbouring modules.

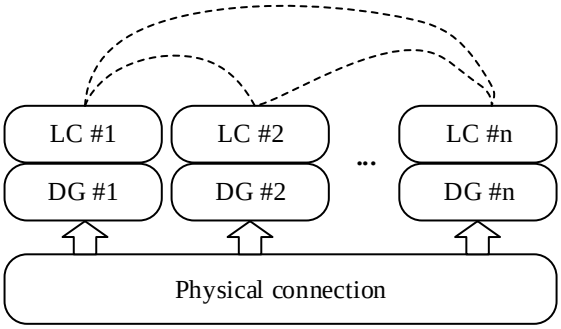

Figure 21. Operation principle of distributed control

The main advantage of this approach is that the system can maintain full functionality, even if the failure of some communication links occurs. Therefore, distributed control is immune to a single point of failure.

However, differently from centralized control, the information directly exchanged between the local controllers can contain only locally available variables. In other words, if the two units are not connected directly by the communication link, they do not have direct access to each other's data and their observation of the whole system is limited.

3.3.3 Decentralized control

Without the use of external communication among local controllers, decentralized control uses local measurement to implement local regulation, as shown in Figure 22. If the failure of one module occurs, the remaining modules can still contribute to power sharing according to their local droop settings. Thus, system reliability is increased. Since communication links among the sources and an additional centralized controller are not needed, each parallel module can work independently relying on the local measurements and controllers.

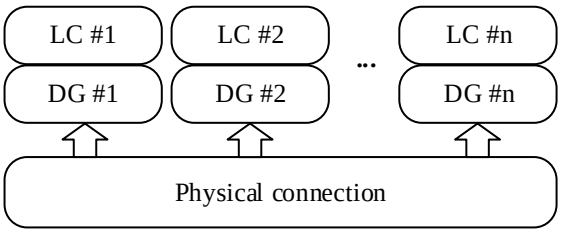

Figure 22. Operation principle of decentralized control

Droop control was firstly employed for AC systems as decentralized control due to no

need for communication lines. Now, it has been widely accepted for DC systems similarly. It utilizes a “virtual resistance” to achieve current sharing. In the DC system, a relationship between current and voltage is built to realise the “virtual resistance” character.

Generally, droop control can be classified into voltage (including V-I and V-P strategy) and current mode (including I-V and I-P strategy) which are shown in Figure 23 a-d respectively. However, the power of the converter is almost proportional to the output current when small voltage errors are considered. Hence, for voltage and current mode droop control, only V-I and I-V strategy will be discussed in this section.

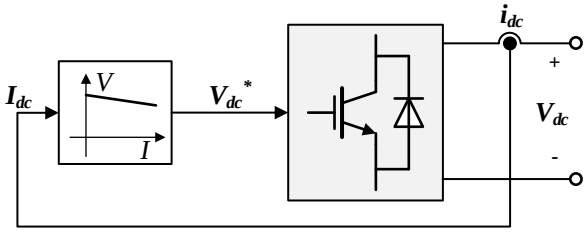

(a)

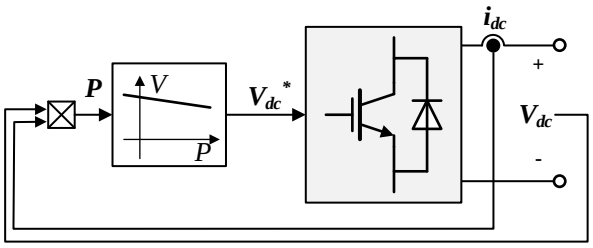

(b)

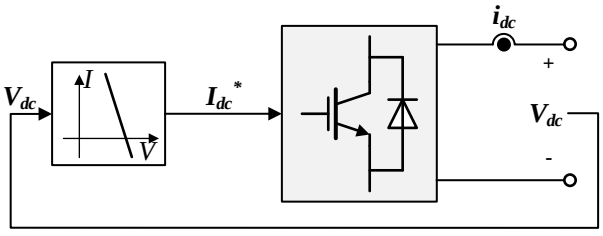

(c)

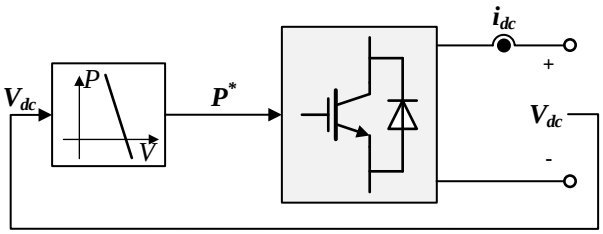

(d)

Figure 23. Droop characteristic. (a) V-I droop. (b) V-P droop. (c) I-V droop. (d) P-V droop.

3.3.3.1 Voltage-mode approach

Voltage mode droop control uses measured branch current to generate voltage reference. The calculation of reference for the voltage controller is as follow:

$$V_{dci}^{*} = V_{dc}^{*} - k_{di} I_{dci} \tag{26}$$

where *i* represents the index of each converter, V_{dci}^{*} is the calculated voltage reference for the *i*th converter, V_{dc}^{*} is the rated voltage, k_{di} is the droop coefficients in voltage-mode droop controllers of the *i*th converter, while I_{dci} is the output current of the *i*th converter.

Figure 24 shows the diagram of the V-I droop control curve when three converters are sharing the same DC bus voltage (V_{dci}) are considered. Then, the power sharing ratio among three converters as obtained from Figure 24 is as expressed in (27).

$$I_{dc1} : I_{dc2} : I_{dc3} = \frac{1}{k_{d1}} : \frac{1}{k_{d2}} : \frac{1}{k_{d3}} \tag{27}$$

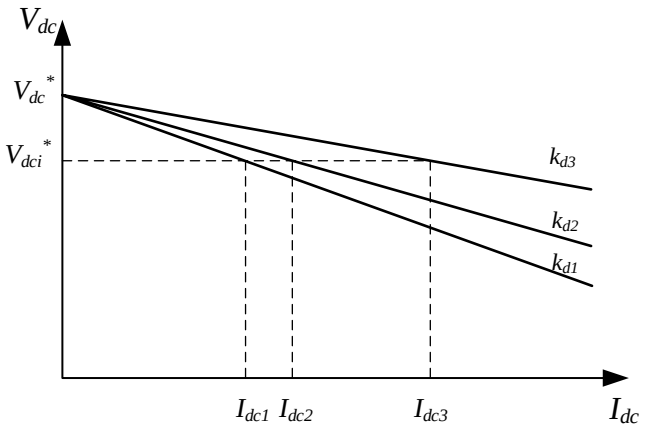

Figure 24. Power sharing characters of V-I droop control curve.

However, when considering the voltage drop on cables, the DC bus voltage in steady-state can be expressed as follows:

$$V_b = V_{dci} - I_{dci}R_i = V_{dc}^* - \left(k_{di} + R_i\right) I_{dci} \tag{28}$$

where V_b is the voltage of the common DC bus. R_i is cable resistance of converter #i. Then the current sharing ratio among sources can be rewritten as expressed in (29).

$$I_{dc1} : I_{dc2} : I_{dc3} = \frac{1}{k_{d1} + R_1} : \frac{1}{k_{d2} + R_2} : \frac{1}{k_{d3} + R_3} \tag{29}$$

It can be inferred that both droop gain and line resistance will influence the power sharing ratio, i.e., upgrading the droop gain or line resistance will decrease the power output of the source.

3.3.3.2 Current-mode approach

For current-mode droop control, the output current reference is obtained by the local voltage measurement and is as expressed in (30).

$$I_{dci}^* = \frac{V_{dc}^* - V_{dci}}{k_{di}} \tag{30}$$

Figure 25 shows the current sharing concept when voltage drop on cable is ignored and the current sharing ratio among the sources is as expressed in (31).

$$I_{dc1} : I_{dc2} : I_{dc3} = \frac{1}{k_{d1}} : \frac{1}{k_{d2}} : \frac{1}{k_{d3}} \tag{31}$$

where k_{di} is the droop gain for the ith local controller.

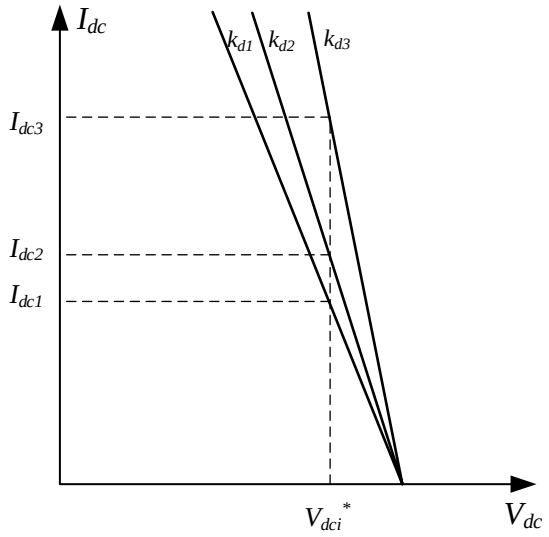

Figure 25. Power sharing characters of I-V droop control curve.

When voltage drop on cable is considered, current sharing among 3 subsystems can be written as in (32).

$$I_{dc1} : I_{dc2} : I_{dc3} = \frac{1}{k_{d1} + R_1} : \frac{1}{k_{d2} + R_2} : \frac{1}{k_{d3} + R_3} \tag{32}$$

Based on the aforementioned analysis, in both current-mode and voltage-mode droop-controlled systems the ratio of the source powers is not as desired due to cable resistances.

As expressed in (29) and (32), increasing droop coefficient (k_{d1}, k_{d2}, and k_{d3}) is the way to eliminate power sharing error. However, the voltage regulation performance is poor with this approach, i.e., the voltage drop is high under high droop gains.

-

4 Summary

A detailed modal analysis of the DC grid onboard aircraft has been performed in this chapter. The PMSG based generation system provides the electrical power from the

engine shaft to the DC bus. ESS provides extra power when an emergency occurs. Resistive and constant power load are also introduced.

After modal analysis of each component, the control method is discussed. For each subsystem such as PMSG and ESS, the local controller is analysed firstly.

Then power sharing control is introduced to coordinate the aircraft electrical power system (EPS). Centralized control and distributed control show better performance because of proper coordination and leadership in small or medium scale system. To avoid failure due to communication, decentralised control can achieve high reliability, modularity and only depends on the local variables. However, the droop coefficient should be carefully chosen to balance the trade-off between voltage drop and power sharing accuracy.

5 Reference

[1] K.J. Karimi, "The role of power electronics in more-electric airplanes (MEA)," presented at the Workshop on Computers in Power Electronics, 2006.

[2] E. Q. Richard, Jr., "More Electric Aircraft," 1993.

[3] I. Moir and A. Seabridge, *Aircraft Systems: mechanical, electrical, and avionics subsystems integration* 3rd ed.: John Wiley & Sons, 2008.

[4] M. Sinnett, "787 No-Bleed Systems: saving fuel and enhancing operational efficiencies," *Boeing Aero Mag*., vol. 4, pp. 6–11, 2007.

[5] P. Wheeler and S. Bozhko, "The More Electric Aircraft: Technology and challenges.," in *IEEE Electrification Magazine*, vol. 2, no. 4, pp. 6-12, Dec. 2014

[6] B. H. Nya, J. Brombach, and D. Schulz, "Benefits of higher voltage levels in aircraft electrical power systems," in *Proc. Electrical Systems for Aircraft, Railway and Ship Propulsion (ESARS)*, Bologna, Oct. 2012, pp. 1–5. 230.

[7] N. Mohan, W. P. Robbins, T. M. Undeland, R. Nilssen, and O. Mo, "Simulation of power electronic and motion control systems-an overview," *Proceedings of the IEEE*, vol. 82, pp. 1287-1302, 1994.

[8] S. V. Bozhko, T. Wu, C. I. Hill, and G. M. Asher, "Accelerated simulation of complex aircraft electrical power system under normal and faulty operational

scenarios," in *IECON 2010 - 36th Annual Conference on IEEE Industrial Electronics Society*, 2010, pp. 333-338.

[9] M. O. Martin R. Kuhn, Loic Raulin, "A Mulit Level Approach for Aircraft Electrical System Design," presented at the International Modelica Conference, 2008.

[10] S. Chiniforoosh, J. Jatskevich, A. Yazdani, V. Sood, V. Dinavahi, J. A. Martinez, and A. Ramirez, "Definitions and Applications of Dynamic Average Models for Analysis of Power Systems," *Power Delivery, IEEE Transactions on*, vol. 25, pp. 2655-2669, 2010.

[11] S. Jian, "Unified averaged switch models for stability analysis of large distributed power systems," in *Applied Power Electronics Conference and Exposition, 2000. APEC 2000. Fifteenth Annual IEEE*, pp. 249-255, 2000.

[12] B. Lehman and R. M. Bass, "Switching frequency dependent averaged models for PWM DC-DC converters," *Power Electronics, IEEE Transactions on*, vol. 11, pp. 89-98, 1996.

[13] P. C.Krause, O. Wasynczuk, and S. D. Sudhoff, *Analysis of electric machinery and dirve systems*: Wiley-interscience, 2002.

[14] S. V. Bozhko, T. Wu, T. Yang, and G. M. Asher, "More-electric aircraft electrical power system accelerated functional modeling," in *Power Electronics and Motion Control Conference (EPE/PEMC), 2010 14th International*, 2010, pp. T9-7-T9-14.

[15] T. Wu, S. Bozhko, G. Asher, and P. Wheeler, "Fast Reduced Functional Models of Electromechanical Actuators for More-Electric Aircraft Power System Study," *SAE Technical Paper 2008-01-2859*, 2008.

[16] T. Wu, S. V. Bozhko, G. M. Asher, and D. W. P. Thomas, "Accelerated functional modeling of aircraft electrical power systems including fault scenarios," in *Industrial Electronics, 2009. IECON '09. 35th Annual Conference of IEEE*, 2009, pp. 2537-2544.

[17] Cleansky. AEGART Project Summary. Available: http://cordis.europa.eu/result/rcn/143557_en.html. Accessed: 11/11/2015.

[18] G. Buticchi, L. Costa and M. Liserre, "Improving system efficiency for the more electric aircraft: A look at dc/dc converters for the avionic onboard dc microgrid," *IEEE Industrial Electronics Magazine*, vol. 11, no. 3, pp. 26-36, 2017.

[19] R. Huggins, Energy Storage: Fundamentals, Materials and Applications (Second Edition), Switzerland: Springer International Publishing, 2016, p. 509.

[20] H. Chen, X. Zhang, J. Liu and C. Tan, "Compressed air energy storage," in *Energy Storage-Technologies and Applications*, InTech, 2013, pp. 101-112.

[21] T. Zhang, J. Mao, X. Liu, M. Xuan, K. Bi, X. L. Zhang, J. Hu, J. Fan, S. Chen and G. Shao, "Pinecone biomass-derived hard carbon anodes for high-performance sodium-ion batteries," *Royal Society of Chemistry Advances*, vol. 7, no. 66, pp. 41504-41511, 2017.

[22] J. Töpler and J. Lehmann, Hydrogen and Fuel Cell, Berlin/Heidelberg, Germany: Springer, 2016.

[23] C. A. Ramos-Paja, A. Romero, R. Giral, J. Calvente and L. Martinez-Salamero, "Mathematical analysis of hybrid topologies efficiency for PEM fuel cell power systems design," *International Journal of Electrical Power & Energy Systems*, vol. 32, no. 9, pp. 1049-1061, 2010.

[24] J. Carroquino, R. Dufo-López and J. L. Bernal-Agustín, "Sizing of off-grid renewable energy systems for drip irrigation in Mediterranean crops," *Renewable energy*, vol. 76, pp. 566-574, 2015.

[25] Zhao, H., Hou, Y., Zhu, Y., Chen, L. and Chen, S, "Experimental study on the performance of an aircraft environmental control system," *Applied Thermal Engineering*, vol. 29, no. 16, pp.3284-3288, 2009.

[26] Jiang, Hongsheng, Sujun Dong, and Helin Zhang. "Energy efficiency analysis of electric and conventional environmental control system on commercial aircraft." in *2016 IEEE International Conference on Aircraft Utility Systems (AUS)*, pp. 973-978, 2016.

[27] D. Barater *et al*., "Multistress Characterization of Fault Mechanisms in Aerospace Electric Actuators," in *IEEE Transactions on Industry Applications*, vol. 53, no. 2, pp. 1106-1115, March-April 2017.

[28] S. S. Yeoh, M. Rashed, M. Sanders and S. Bozhko, "Variable-Voltage Bus Concept for Aircraft Electrical Power System," in *IEEE Transactions on Industrial Electronics*, vol. 66, no. 7, pp. 5634-5643, July 2019.

[29] I. Moir and A. Seabridge, *Aircraft Systems: Mechanical, Electrical and Avionics Subsystems Integration*. New York, NY, USA: Wiley, 2008.